

## Original Article

# A Low-Sulfidation Epithermal Mineralization in the River Reef Zone, the Poboya Prospect, Central Sulawesi, Indonesia: Vein Textures, Ore Mineralogy, and Fluid Inclusions

Tomy Alvin RIVAI,<sup>1</sup>  Kotaro YONEZU,<sup>1</sup> SYAFRIZAL,<sup>2</sup> Kenzo SANEMATSU,<sup>3</sup> Damar KUSUMANTO,<sup>4</sup> Akira IMAI<sup>1</sup> and Koichiro WATANABE<sup>1</sup>

<sup>1</sup>Department of Earth Resources Engineering, Kyushu University, Fukuoka, <sup>3</sup>Geological Survey of Japan, AIST, Tsukuba, Ibaraki, Japan, <sup>2</sup>Faculty of Mining and Petroleum Engineering, Bandung Institute of Technology, Bandung and <sup>4</sup>PT Bumi Resources Minerals, Tbk, Jakarta, Indonesia

## Abstract

The Poboya Prospect lies along the North Northwest - South Southeast Palu-Koro Fault Zone in the central part of the West Sulawesi Arc. The geology of the area consists of the Palu Metamorphic Complex overlain by the Paleogene-Neogene Tinombo Formation of volcanosedimentary rocks, the Celebes Molasse sediment, and Late Cenozoic granitic rocks. Petrography, scanning electron microscope with energy-dispersive spectrometry (SEM-EDS), electron probe microanalyzer (EPMA), and fluid inclusion microthermometry were carried out to examine vein textures, ore mineralogy, and characteristics of the ore-forming fluid responsible for mineralization in the River Reef Zone, the Poboya Prospect. Textures of quartz-carbonate veins in the River Reef Zone include massive micro-comb, moss, colloform, crustiform, mosaic, feathery, flamboyant, lattice bladed, ghost bladed, parallel bladed, and saccharoidal textures representing primary growth, recrystallization, and replacement. The homogenization temperature and fluid salinity are 240–250°C and 0.3–0.7 wt% NaCl eq., respectively. Ore minerals precipitated in the early stage consist of electrum, naumannite-aguilarite, chalcopyrite, pyrite, marcasite, sphalerite, and pyrrhotite. Apart from pyrrhotite, these ore minerals were also precipitated in the late stage along with selenopolybasite, freibergite, argyrodite, pyrargyrite, and galena. Selenium more preferably occurs as the crystallographic replacement of sulfur in naumannite-aguilarite, argyrodite, pyrargyrite, selenopolybasite, and freibergite instead of as independent selenide minerals. The low-sulfidation epithermal deposit in the River Reef Zone, the Poboya Prospect, illustrates the potential of the West Sulawesi Arc, particularly along the Palu-Koro Fault Zone, to host epithermal gold mineralization.

**Keywords:** epithermal gold mineralization, fluid inclusion, Indonesia, ore mineralogy, sulawesi, vein texture.

Received 29 October 2018. Revised 15 April 2019. Accepted for publication 10 May 2019.

Corresponding author: T. A. Rivai, Department of Earth Resources Engineering, Kyushu University, 744 Motooka, Nishiku, Fukuoka 819-0395, Japan. Email: tomyalvinrivai@mine.kyushu-u.ac.jp

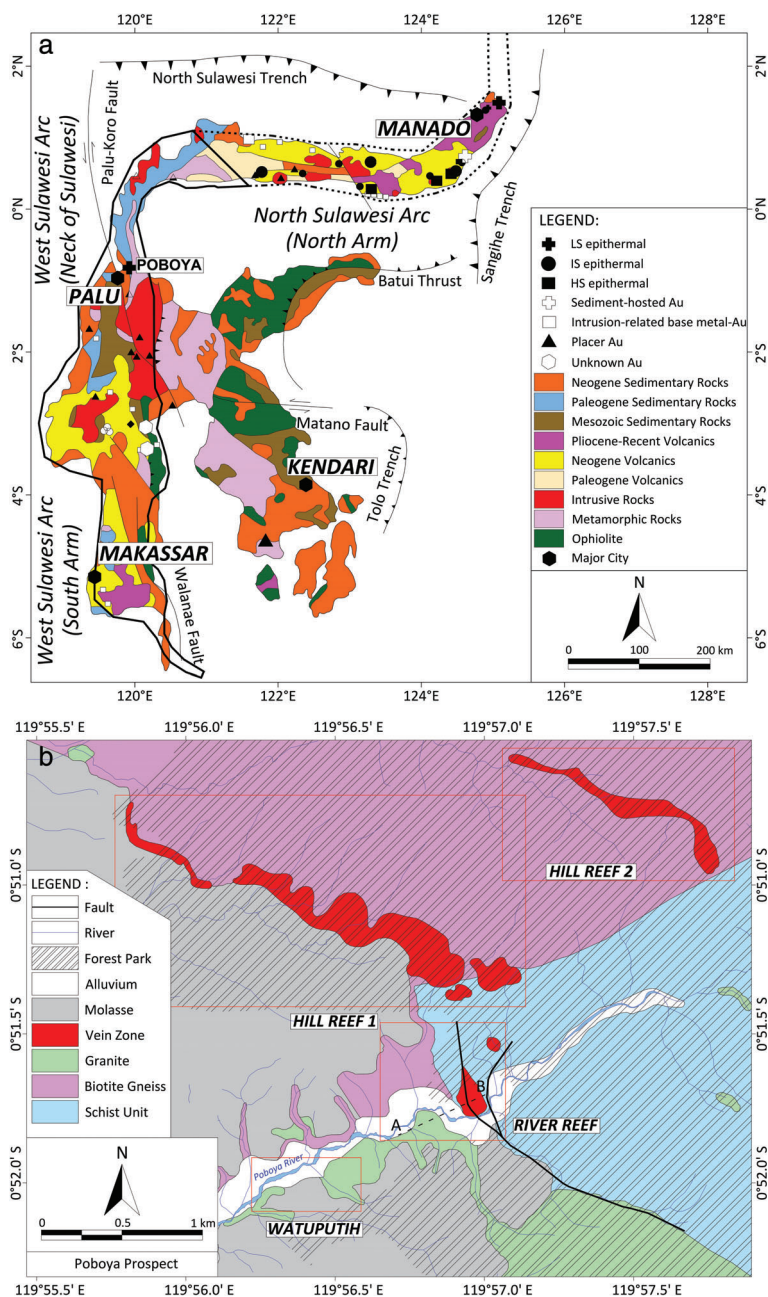


**Fig. 1** (a) Geological map of Sulawesi showing distribution of gold deposits in the island (modified after Van Leeuwen & Pieters, 2011). Gold deposits in Sulawesi are distributed in the West and North Sulawesi Arcs (modified after Garwin *et al.*, 2005) dominated by metamorphic and volcanic terranes, respectively. (b) Geological map of the Poboja Prospect (modified from Wajdi *et al.*, 2012; Syafrizal *et al.*, 2017). River Reef Zone, Hill Reef Zone 1, and Hill Reef Zone 2 extend in a NW-SE strike, along with the occurrences of schist unit, biotite gneiss, granite, molasse, and alluvium sediments. Dashed line A-B represents the location of a cross section illustrated in Figure 2.

## 1. Introduction

The Poboja Prospect is located approximately 12 km from the Palu City, Central Sulawesi, Indonesia (Fig. 1a). Three vein zones have been outlined in this prospect (Wajdi *et al.*, 2012): the River Reef Zone (RRZ), the Hill Reef 1 Zone (HRZ-1), and the Hill Reef 2 Zone (HRZ-2). A series of drilling campaigns in the RRZ conducted from 1996 to 2012, with a total depth

of 11,400 m, succeeded in finding orebodies hosting 18 million metric tons of ore at 3.4 g/t Au (van Leeuwen & Pieters, 2011).

In terms of the tectonic setting, the Poboja Prospect lies on the West Sulawesi Arc, characterized as a collisional setting, metamorphic rock-dominated terrane, and is therefore less favorable for gold exploration (van Leeuwen, 1994; Wajdi *et al.*, 2012). This arc differs from the North Sulawesi Arc, characterized as an

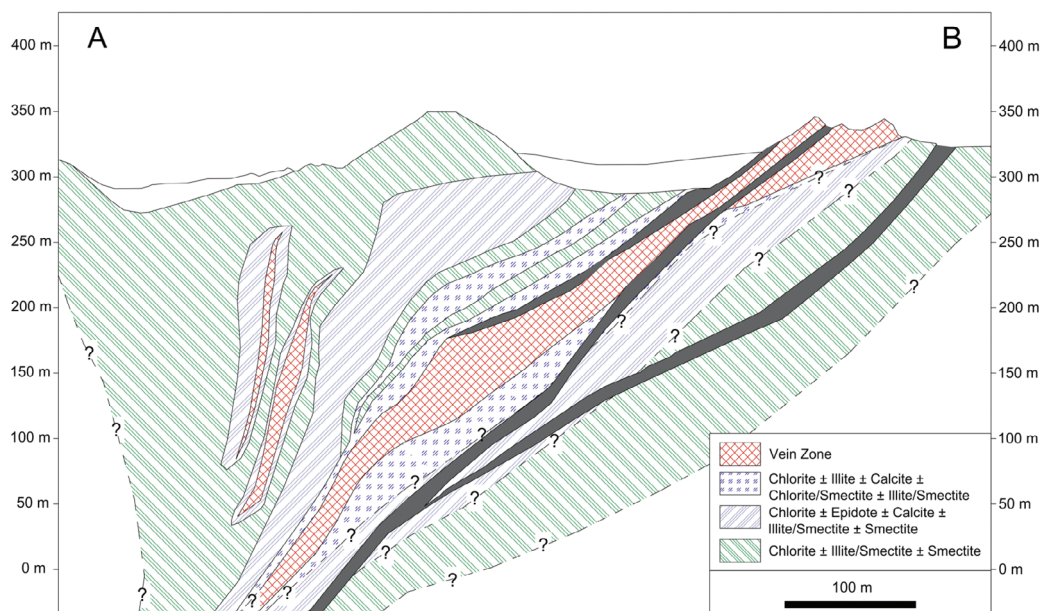


**Fig. 2** Hydrothermal alteration zoning in the River Reef Zone (Syafrizal *et al.*, 2017). From the vein zone outward, hydrothermal alteration assemblages are chlorite-illite-chlorite/smectite-illite/smectite-calcite, chlorite-epidote-calcite-illite/smectite-smectite, and chlorite-illite/smectite-smectite. The cross section above depicts hydrothermal alteration along line A–B in Figure 1b.

island arc setting with widely distributed volcanic rocks (Carlile *et al.*, 1990; Kavalieris *et al.*, 1992) and with several gold mineralization deposits (e.g. Kavalieris *et al.*, 1990; Perelló, 1994; Turner *et al.*, 1994; Wisanggono *et al.*, 2011). Notwithstanding the unattractiveness of the West Sulawesi Arc for gold exploration, the discovery of the Poboya Prospect and several occurrences of gold placer deposits along the Palu-Koro Fault Zone (PKFZ) may shift the perspective regarding gold exploration in this arc (Fig. 1a).

With regard to the potential of the West Sulawesi Arc to host gold deposits, mineralization in the RRZ offers an opportunity to study gold metallogensis in this arc. A better understanding of the deposit characteristics and genesis provides insights on gold exploration in the West Sulawesi Arc. In this paper, we present our work on vein textures, ore mineralogy, and fluid inclusion microthermometry in the RRZ.

## 2. Geologic background

### 2.1 Regional geology

The Poboya Prospect is situated in the central part of the West Sulawesi Arc (Fig. 1a). The base of this area

is known as the Palu Metamorphic Complex (PMC), consisting of biotite gneiss, biotite schist, amphibolite, and amphibolite schist. Several higher-grade metamorphic rocks, including granulite and eclogite and garnet peridotite, are also present (Helmerts *et al.*, 1990). This complex was derived from metasediments and metagranitoids originating from Australia, metabasites of mid-oceanic ridge basalt affinity, and Sundaland origin rocks (van Leeuwen *et al.*, 2007).

The PMC is overlain by the volcanosedimentary Tinombo Formation deposited during the Paleogene and Neogene. The PMC and the Tinombo Formation were intruded by Late Neogene granitic rocks. A rapid exhumation at an average rate of 0.7–1.0 mm year<sup>-1</sup> occurred in the central part of the West Sulawesi Arc, which led to the deposition of the Celebes Molasse sediment (van Leeuwen *et al.*, 2016). This sediment is distributed on the flank of the uplifted metamorphic complex along the neck of Sulawesi (van Leeuwen & Muhandjo, 2005).

Geological structures in the central part of the West Sulawesi Arc are controlled by the North Northwest–South Southeast PKFZ (Katili, 1970). The PKFZ extends from the tip of the Matano Fault in the south and terminates in the western-most side of the North Sulawesi Trench. Other structures are subparallel to

the PKFZ (Sukanto *et al.*, 1973). In the Palu area, the PKFZ occurs as a pull-apart basin hosting gold mineralization in the Poboya Prospect (Wajdi *et al.*, 2012).

## 2.2 Local geology

According to Wajdi *et al.* (2012), lithology in the Poboya Prospect is divided into two domains with respect to the strike of the vein zone at the HRZ-1. In the northeastern portion, the lithology consists of gneiss and schist. To the southwest, the gneiss and schist were intruded by monzonite and widely covered by molasse sediment, which was the product of Quaternary rapid uplift in the neck of Sulawesi (van Leeuwen & Muhandjo, 2005). Recent alluvium is deposited along the Poboya riverbank (Fig. 1b).

Syafrizal *et al.* (2017) reclassified the lithology in the RRZ based on petrographic and geochemical studies. The monzonite was assessed as a magnesian arc granite that lies on the trend of calcic and calc-alkaline borderline. The gneiss was renamed biotite gneiss derived from granitic rocks. The schist is dominated by biotite schist originating from psammitic rocks. Hornblende schist and biotite schist with feldspar porphyroblasts are present within the biotite schist.

Hydrothermal alteration in the RRZ (Syafrizal *et al.*, 2017) is zoned outward from the chlorite-illite-interstratified chlorite/smectite-interstratified illite/smectite-calcite zone through the chlorite-epidote-calcite-interstratified illite/smectite-smectite zone to the chlorite-interstratified illite/smectite-smectite zone (Fig. 2). These alteration mineral assemblages suggest that the hydrothermal fluids were in near-neutral pH condition. In addition, the alteration mineral assemblages and their zonation are consistent with general alteration patterns occurring in low-sulfidation epithermal deposits.

## 3. Materials and methods

A total of 41 samples were collected from four boreholes in the RRZ: POBO0036 (16 samples), POBO0044 (7 samples), POBO0040 (10 samples), and DD96PA02 (8 samples; Fig. 3). Of these samples, 27 polished sections, 10 doubly polished thin sections, and 13 thin sections were prepared and analyzed using a polarizing microscope NIKON E600POL in order to examine their ore mineralogy and vein textures. This study was conducted in Kyushu University, Japan.

Ore minerals from six samples were further analyzed by a scanning electron microscope with energy-dispersive spectrometry (SEM-EDS) JSM-6610LV and a field emission electron probe microanalyzer (EPMA) JEOL JXA-8530F in order to obtain the chemical composition of the ore minerals. The standards used in EPMA were JEOL standards of gold and silver. Quantitative analysis was performed at an accelerating voltage of 20 kV and a probe current of 20 kV. Crystal PETH was used to measure the intensity of the X-ray lines of Au $M\alpha$  and Ag $L\alpha$ . The counting times for these elements were 20s at the peak and 10s at the background. This study was carried out in the Geological Survey of Japan.

Fluid inclusion microthermometry was carried out to obtain homogenization temperature ( $T_h$ ) and final ice-melting temperature ( $T_m$ ). Salinity was estimated from the  $T_m$  using the equation of freezing temperature depression of Bodnar (1993). Measurements were conducted using heating and cooling stages of LINKAM THMS600 (range of measurement temperature:  $-196^\circ$  to  $600^\circ\text{C}$ ) in Kyushu University, Japan. The temperature increment ratio used was sequentially reduced from 20 to  $1^\circ\text{C min}^{-1}$  as the stage temperature became closer to  $T_h$  and  $T_m$ .

## 4. Results

### 4.1 Vein textures

The veins observed in the RRZ have an individual thickness of less than 1 cm up to approximately 10 m (van Leeuwen & Pieters, 2011). The veins are mainly composed of quartz and calcite with variable grain size and mineral habits. Quartz was observed as cryptocrystalline [hereafter referred to as chalcedony (Phillips & Griffen, 1981)], microcrystalline, and crystalline in terms of its size (Bates & Jackson, 1987), while calcite was observed as platy and irregular, coarse grains (Thompson & Thompson, 1996). When there was a lack in crystallographic structure, silica was present as amorphous silica (Morrison *et al.*, 1990). The coexistence of amorphous silica, quartz, and calcite in the veins results in various textures observed in the RRZ, including massive, micro-comb, moss, colloform, crustiform, mosaic, feathery, flamboyant, lattice bladed, ghost bladed, parallel bladed, and saccharoidal textures (Morrison *et al.*, 1990). The dominant textures are massive, micro-comb, mosaic, lattice bladed, ghost bladed, and parallel bladed textures, while the other textures are not as dominant.

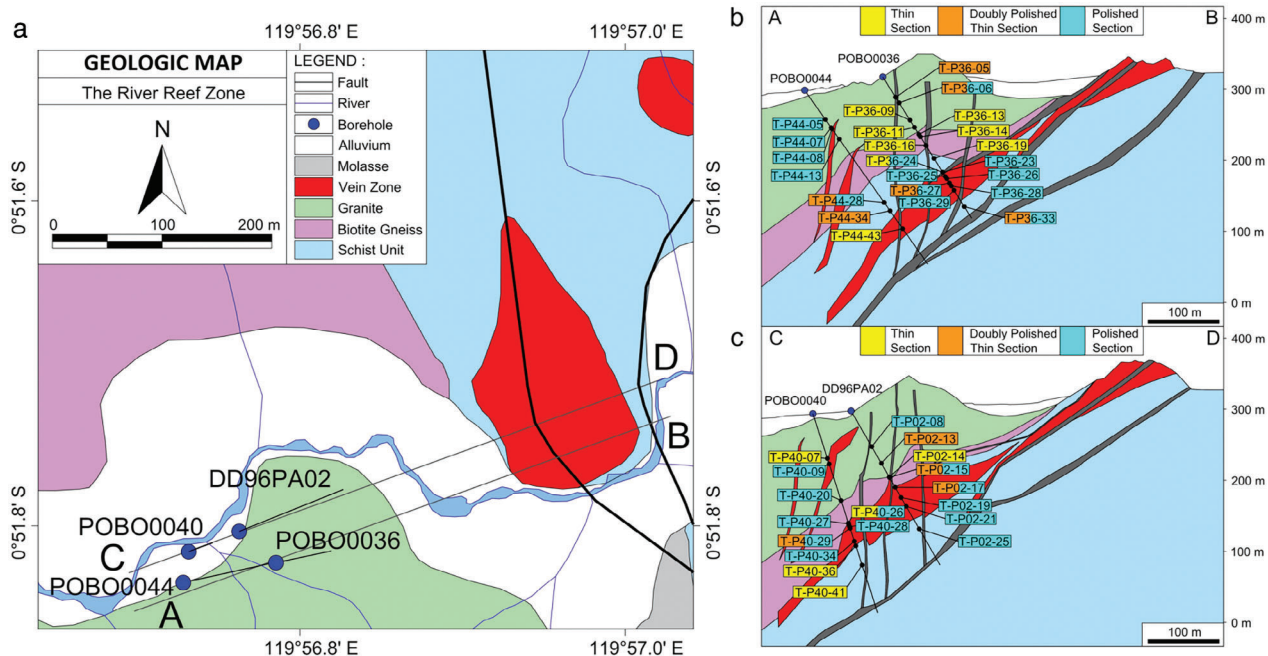


**Fig. 3** (a) Borehole locations in the River Reef Zone from which samples were collected. (b) Cross section along line A–B and sample locations from boreholes POBO0036 and POBO0040. (c) Cross section along line C–D and sample locations from boreholes POBO0040 and DD96PA02.

The massive texture is displayed by chalcedony and minor calcite (Fig. 4a). Parallel-oriented, prismatic quartz exhibiting a micro-comb texture was frequently observed to flank massive chalcedony and minor calcite along the vein zone (Fig. 4a). Vugs bounded by euhedral, crystalline quartz growing toward the center of the voids were observed in this texture. Occasionally, the massive texture was exhibited by irregular, coarse-grained calcite with minor microcrystalline quartz. Massive chalcedony was observed next to the massive texture exhibited by coarse-grained calcite with microcrystalline quartz (Fig. 4b). Amorphous silica, chalcedony, and microcrystalline quartz appear to have been recrystallized, resulting in interpenetrating irregular, crystalline quartz showing a mosaic texture (Fig. 4c).

The lattice bladed texture was observed as intersecting blades of platy calcite with polyhedral interstices. The interstices were filled with prismatic, microcrystalline quartz, which grew perpendicularly to the edge of platy calcite. Chalcedony and microcrystalline quartz present in the interstices of platy calcite and prismatic quartz appear to have partially replaced platy calcite (Fig. 4d). Besides showing a lattice bladed texture, intersecting platy calcite is also

distributed on aggregates of microcrystalline quartz without interstices. This aggregate represents the ghost bladed texture (Fig. 4e). Similar to platy calcite with a lattice bladed texture, platy calcite with this texture has also been partially replaced by quartz. Inclusions in calcite, as well as rhombic cleavages of calcite, are preserved after replacement. Occasionally, platy calcite is arranged in a parallel manner, displaying the parallel bladed texture (Fig. 4f). Replacement of calcite by quartz was also observed in the saccharoidal texture. In this texture, calcite appears as a coarse-grained mineral, while quartz appears as a subhedral prismatic, microcrystalline mineral. Orthogonally arranged quartz crystals demonstrate a reticulated structure (Fig. 4g).

The crustiform texture represents successive bands with individual thickness of up to 2 cm. Each band is composed of quartz and calcite with variable size and habits. Several types of band succession were observed. In the first type, the bands at the edge of the veins are composed of platy calcite, irregular calcite, and microcrystalline quartz of the ghost bladed texture. These bands form an alternation with the bands composed of prismatic, microcrystalline quartz of the micro-comb and chalcedony of the massive textures.

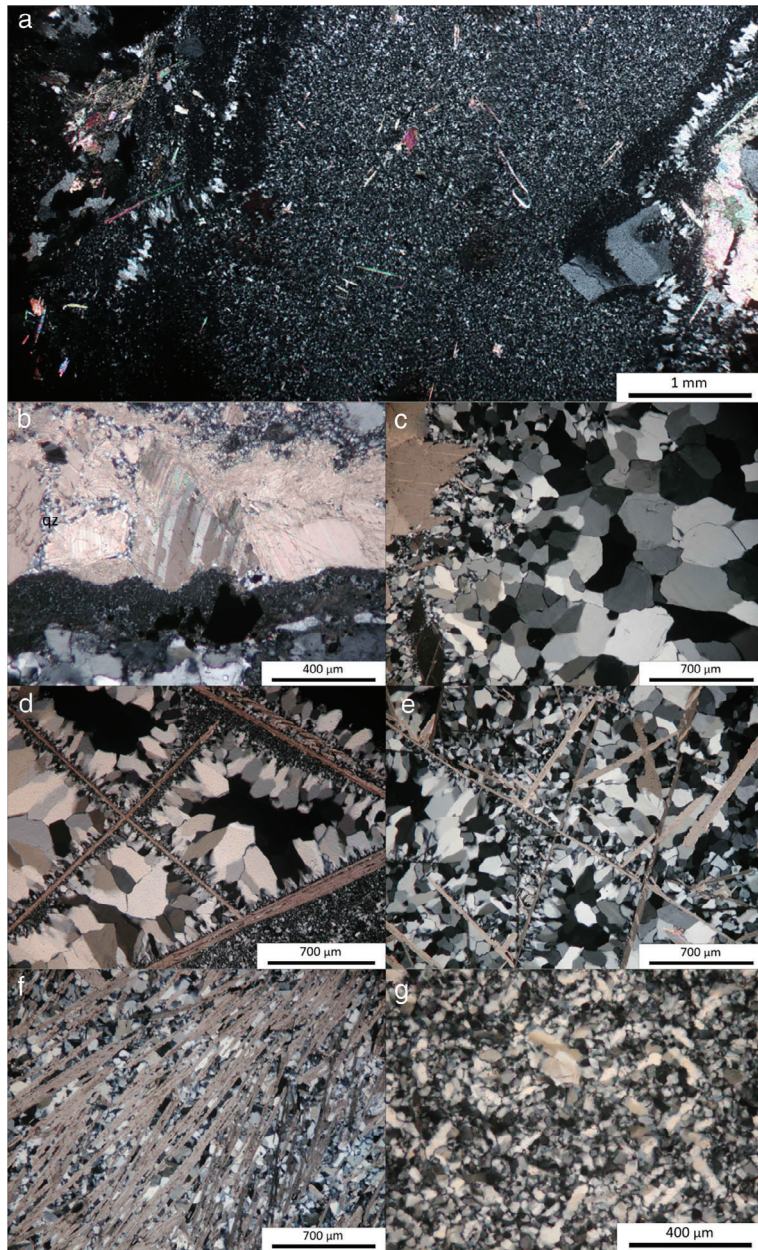


**Fig. 4** (a) Photomicrographs of massive cryptocrystalline quartz and minor platy calcite flanked by micro-comb quartz textures (T-P36-24, POBO0036, depth 158.45 m); (b) coarse, irregular calcite and cryptocrystalline quartz (T-P02-15, DD96PA02, depth 108.10 m); (c) mosaic quartz texture (T-P36-24, POBO0036, depth 158.45 m); (d) lattice bladed calcite and their interstices filled by quartz (T-P44-28, POBO0044, depth 193.45 m); (e) ghost bladed texture of calcite (T-P44-34, POBO0044, depth 207.85 m); (f) parallel bladed texture of calcite (T-P44-43, POBO0044, depth 238.75 m); and (g) saccharoidal quartz texture (T-P36-19, POBO0036, depth 135.55 m).

Toward the center of the veins, crustiform banding comprises the alternating micro-comb quartz layer and moss silica layer. In the moss silica layer, amorphous silica appears as rounded aggregates surrounded by fibrous microcrystalline quartz. The independent spheres of the moss texture of quartz are interconnected, resulting in the colloform texture. In the shallow portion of the vein zone, colloform quartz and micro-comb quartz have recrystallized to form quartz with radial extinction or a flamboyant texture.

Recrystallized colloform also appears as an aggregate of fibrous quartz with splintery extinction or feathery texture (Fig. 5a). The second type is characterized as alternating ghost bladed and massive microcrystalline quartz textures. Platy calcite exhibiting a ghost bladed texture is embedded in chalcedony. Thin colloform bands were seen to interrupt this repetition (Fig. 5b). In the third type, crustiform banding is displayed by the alternating massive microcrystalline quartz and ghost bladed textures showing calcite without being

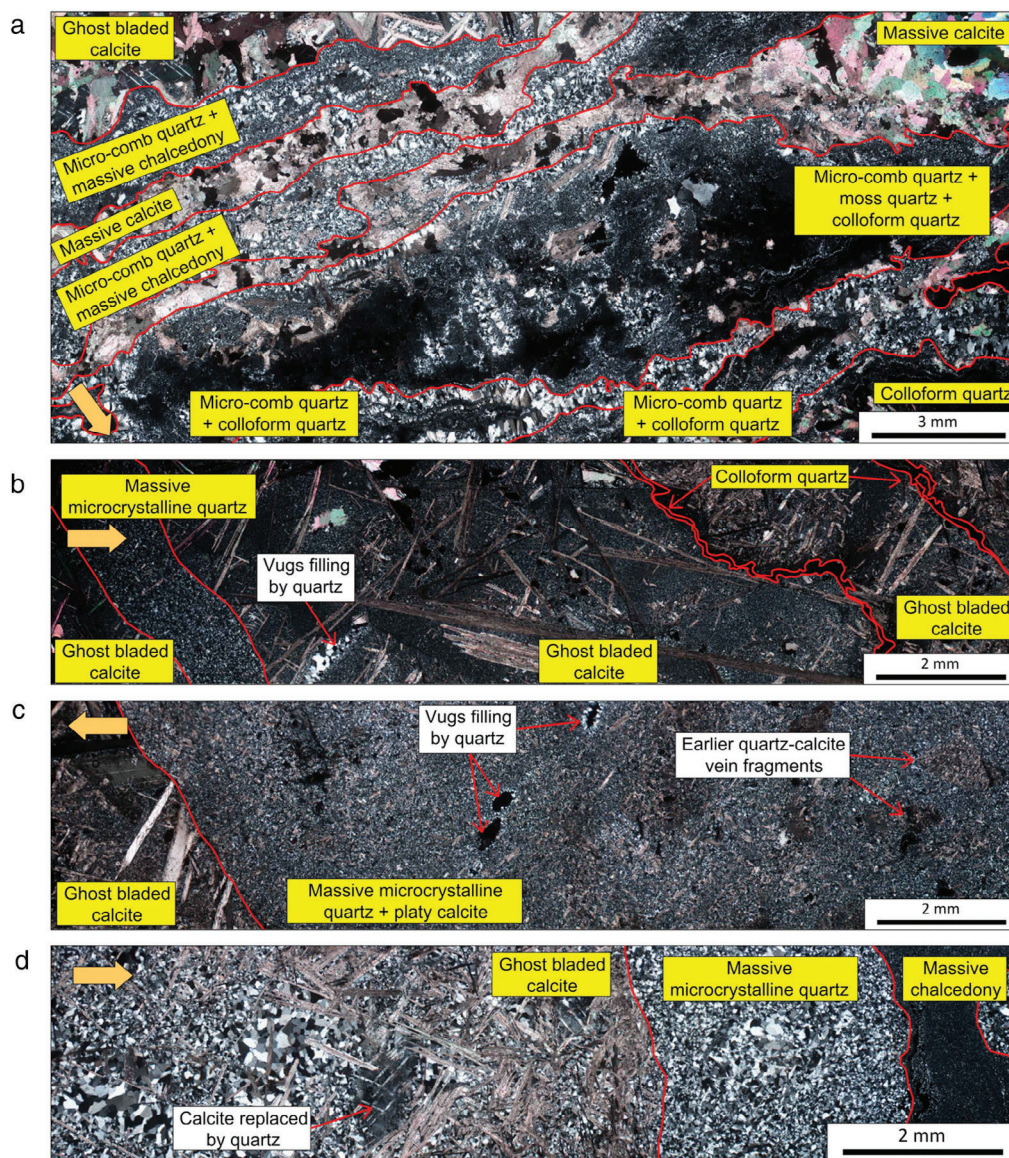


**Fig. 5** Photomicrographs of crustiform textures observed in the River Reef Zone: (a) type 1 (T-P02-13, DD96PA02, depth 104.85 m), (b) type 2 (T-P02-19, DD96PA02, depth 104.60 m), (c) type 3 (T-P02-17, DD96PA02, depth 124.15 m), and (d) type 4 (T-P44-34, POBO0044, depth 207.85 m). Arrows indicate direction toward the center of the veins.

interrupted by colloform bands. In the massive microcrystalline quartz, fine-grained platy calcite and fragments of an earlier massive vein were observed. These fragments contain more calcite than the microcrystalline quartz matrix (Fig. 5c). In the fourth type, the edge of the vein consists of ghost bladed platy calcite embedded on crystalline quartz. This band is succeeded by massive microcrystalline quartz and massive chalcidony bands toward the center of the veins (Fig. 5d).

## 4.2 Ore mineralogy

Ore minerals identified in the RRZ include electrum, naumannite-aguilarite, argyrodite, pyrargyrite, selenopolybasite, freibergite, chalcopryrite, sphalerite, galena, pyrite, marcasite, and pyrrhotite. The occurrence of these minerals is described below, and except electrum, they are grouped into Ag-S-Se minerals, Ag-sulfosalts, base metal sulfide minerals, and Fe-sulfide minerals (Fig. 6).

Electrum is the most prominent Au-bearing mineral in the RRZ and mostly occurs as free grains. It shares simple mutual contacts with other ore minerals, such as

naumannite-aguilarite, selenopolybasite, freibergite, chalcocopyrite, sphalerite, and pyrite. Electrum was also observed as inclusions in pyrite, naumannite-aguilarite,

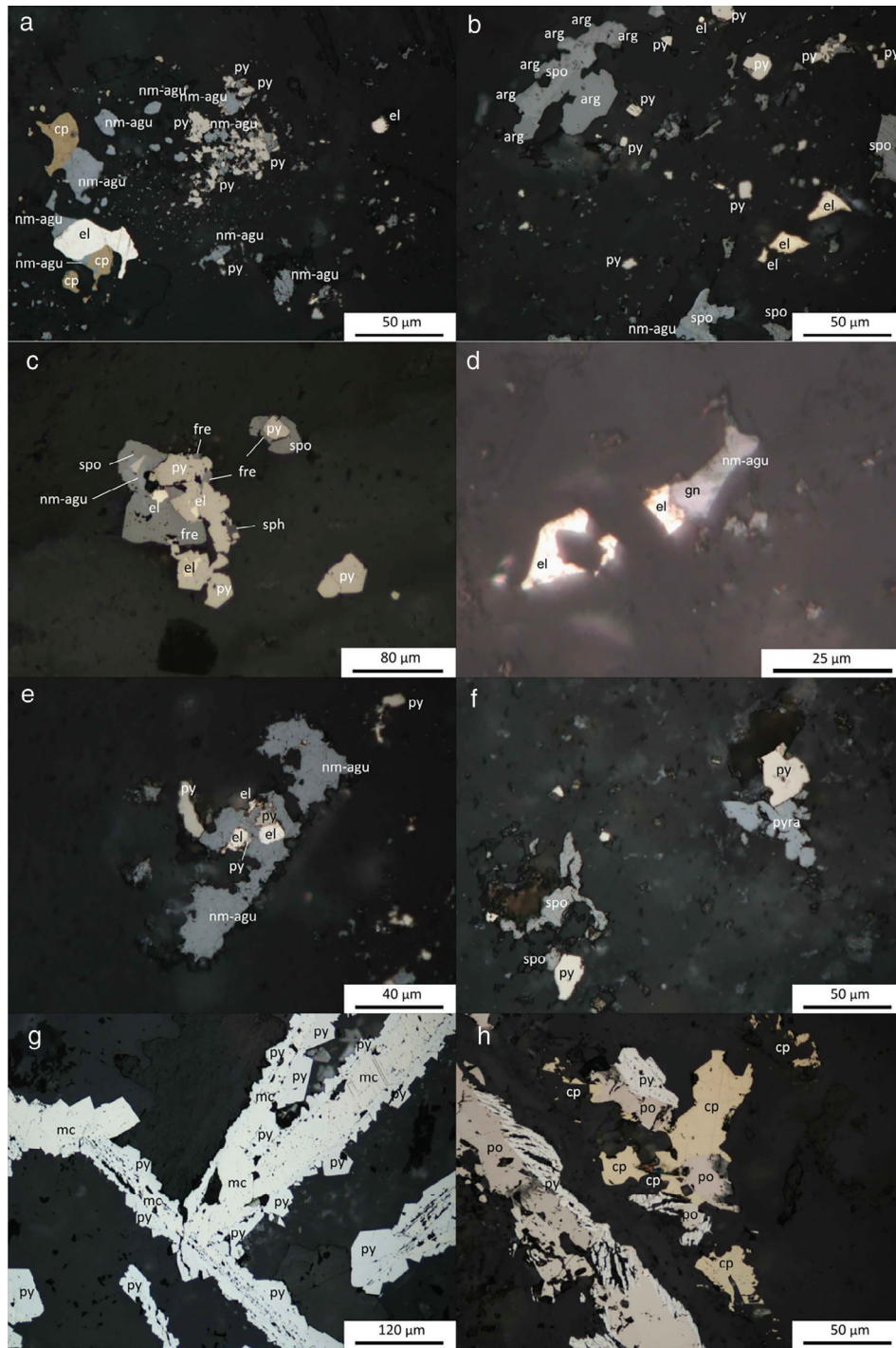


**Fig. 6** Legend on next page.

chalcopyrite, and intergrowth with naumannite-aguilarite, freibergite and selenopolybasite. The size of electrum is up to 50  $\mu\text{m}$ .

Ag-S-Se minerals are the most predominant Ag-bearing minerals in the RRZ. Ag-S-Se minerals belong to naumannite-argentite solid solution, particularly in the range of naumannite-aguilarite composition. Besides being present as free grains, these minerals share simple mutual contacts with electrum, chalcopyrite, selenopolybasite, freibergite, galena, and pyrite. Ag-S-Se minerals were also found to be host minerals for electrum and pyrite inclusions. In addition, Ag-S-Se minerals were observed as randomly oriented inclusions in pyrite.

In addition to Ag-S-Se minerals, Ag is also hosted in Ag-sulfosalts, predominated by selenopolybasite. This mineral shares mutual contacts with electrum, Ag-S-Se minerals, freibergite, sphalerite, and pyrite. Free grains of selenopolybasite are also present. In addition to selenopolybasite, another Ag-sulfosalt was identified as pyrargyrite. Pyrargyrite coexists with pyrite. Silver is contained within freibergite as well. This mineral coexists with electrum, selenopolybasite, and pyrite. A trace amount of argyrodite is also present, and it shares mutual grains with selenopolybasite.

Base metal sulfide minerals present include chalcopyrite, sphalerite, and galena. Among these minerals, chalcopyrite is the most abundant mineral, while sphalerite and galena are present in trace amounts. Chalcopyrite coexists with electrum, naumannite-aguilarite, pyrite, marcasite, and pyrrhotite. It also hosts electrum and pyrite inclusions. Simple mutual contacts were observed between sphalerite and pyrite, as well as among galena, electrum, and naumannite-aguilarite.

Pyrite is the most abundant sulfide mineral. It shares mutual contact with electrum, naumannite-

aguilarite, selenopolybasite, pyrargyrite, freibergite, chalcopyrite, sphalerite, marcasite, and pyrrhotite. As inclusion minerals, pyrite was observed within electrum, naumannite-aguilarite, and chalcopyrite. In addition, pyrite hosts electrum and naumannite-aguilarite as inclusions. Pyrrhotite and marcasite occur as minor iron sulfides. Marcasite shares mutual contact with pyrite, while pyrrhotite shares mutual contact with pyrite and chalcopyrite.

Precipitation of the ore minerals in the RRZ is divided into early and late stages. The early stage is marked by an ore mineral assemblage of electrum, naumannite-aguilarite, chalcopyrite, pyrite, marcasite, sphalerite, and pyrrhotite embedded in quartz. This stage was terminated by barren quartz-calcite veinlets. The late stage is characterized by more various ore minerals comprising electrum, naumannite-aguilarite, selenopolybasite, freibergite, sphalerite, pyrite, marcasite, argyrodite, pyrargyrite, chalcopyrite, and galena. These ore minerals were precipitated along with quartz and calcite and terminated by the precipitation of microcrystalline quartz and pyrite. Most of Ag-bearing minerals were precipitated after electrum and pyrite.

### 4.3 Ore minerals chemistry

Semiquantitative analysis of the chemical composition of ore minerals were carried out on electrum, Ag-S-Se minerals, Ag-sulfosalts, Ag-bearing chalcopyrite, and sphalerite. Proportions of Au and Ag in electrum in the early and late stages of mineralization were further determined by quantitative analysis. The chemical composition of these minerals was determined on polished sections using an SEM-EDS and an EPMA for semiquantitative and quantitative analyses, respectively.

**Fig. 6** (a) Photomicrographs of electrum, naumannite-aguilarite, Ag-bearing chalcopyrite, and pyrite in the early stage (T-P40-29, POBO0040, depth 169.55 m); (b) free grains of electrum and spotty mutual grain relationship between selenopolybasite, argyrodite, and naumannite aguilarite in the late stage (T-P02-15, DD96PA02, depth 108.10 m); (c) electrum inclusions in pyrite and the intergrowth of naumannite-aguilarite, selenopolybasite, and freibergite with minor occurrence of sphalerite in the late stage (T-P02-15, DD96PA02, depth 108.10 m); (d) free grains of electrum and simple mutual contact between naumannite-aguilarite and galena in the late stage (T-P02-15, DD96PA02, depth 108.10 m); (e) electrum and pyrite inclusions in naumannite-aguilarite in the early stage (T-P40-29, POBO0040, depth 169.55 m); (f) coexistence of pyrargyrite, selenopolybasite, and pyrite in the late stage (T-P02-15, DD96PA02, depth 108.10 m); (g) pyrite overgrowing marcasite in the late stage (T-P02-19, DD96PA02, depth 140.60 m); and (h) pyrite coexisting with pyrrhotite and chalcopyrite in the early stage (T-P40-29, POBO0040, depth 169.55 m). Abbreviations: arg, argyrodite; cp, chalcopyrite; el, electrum; fe, freibergite; gn, galena; mc, marcasite; nm-agu, naumannite-aguilarite; po, pyrrhotite; py, pyrite, pyra; pyrargyrite; sp, sphalerite; spo, selenopolybasite.

**Table 1** Chemical composition of electrum determined by electron probe microanalyzer (EPMA)

No	Sample	Stage	<i>n</i>	Ag (wt%)	Au (wt%)	Total (wt%)	Ag (at%)	Au (at%)	Total (at%)	Empirical formulae
1	T-P40-29	Early	20	52.11	43.11	95.22	68.65	31.35	100.00	Ag <sub>69</sub> Au <sub>31</sub>
2	T-P02-15	Late	20	44.09	55.55	99.64	59.05	40.95	100.00	Ag <sub>59</sub> Au <sub>41</sub>
3	T-P02-17	Late	9	44.02	49.48	93.50	61.49	38.51	100.00	Ag <sub>61</sub> Au <sub>39</sub>
4	T-P40-09	Late	25	44.27	50.70	94.97	61.26	38.74	100.00	Ag <sub>61</sub> Au <sub>39</sub>
5	T-P40-34	Late	14	41.89	54.66	96.55	58.21	41.79	100.00	Ag <sub>58</sub> Au <sub>42</sub>

#### 4.3.1 Electrum

The silver content of electrum in the early stage is 69 at% and that in the late stage ranges from 58 to 61 at% (Table 1).

#### 4.3.2 Ag-S-se minerals

Petruk *et al.* (1974) divided Ag-S-Se minerals according to their S/(S + Se) ratio into naumannite (Ag<sub>2</sub>Se–Ag<sub>2</sub>Se<sub>0.88</sub>S<sub>0.12</sub>), aguilarite (Ag<sub>4</sub>Se<sub>1.05</sub>S<sub>0.95</sub>–Ag<sub>4</sub>Se<sub>0.90</sub>S<sub>1.10</sub>), and acanthite or argentite (Ag<sub>2</sub>Se<sub>0.15</sub>S<sub>0.85</sub>–Ag<sub>2</sub>S). Ag-S-Se minerals with intermediate compositions were classified as naumannite-aguilarite and argentite-aguilarite. Semi-quantitative analysis results show that the S/Se ratio of Ag-S-Se minerals in the RRZ fall within an interval of 0.32–0.42, thus resulting in naumannite-aguilarite composition (Table 2).

#### 4.3.3 Ag-sulfosalts

Ag-sulfosalts in the RRZ include selenopolybasite, argyrodite, pyrargyrite, and freibergite. The Cu/(Cu + Ag) ratio of selenopolybasite is limited to below 0.1 and, hence, excludes pearcite (Hall, 1967). The S/(S + Se) ratio of this mineral ranges from 0.73 to 0.81. A similar S/(S + Se) ratio is observed for argyrodite ranging from 0.73 to 0.80. The S/(S + Se) ratio of pyrargyrite and freibergite is above 0.95 (Table 3).

#### 4.3.4 Ag-bearing chalcopyrite and sphalerite

The results of the semiquantitative analysis show that several grains of chalcopyrite contain Ag. These grains of Ag-bearing chalcopyrite were observed to share mutual contacts with naumannite-aguilarite. Silver in chalcopyrite may be derived from naumannite-aguilarite as it is diffused to form a thin layer of acanthite on the surface of chalcopyrite (Chen *et al.*, 1980). The FeS content of sphalerite in the late stage ranges from 1.8 to 2.3 mol% (Table 4).

### 4.4 Fluid inclusion

Fluid inclusions hosted in calcite associated with the ore minerals (electrum, naumannite-aguilarite, argyrodite, selenopolybasite, pyrargyrite, freibergite, sphalerite, galena, and pyrite) in the late stage of mineralization were observed. Measureable primary fluid inclusions occur as isolated assemblages with size up to approximately 30 µm and have negative, degraded negative, and irregular shapes. The primary fluid inclusions are also present along the growth zone of calcite. However, the size of these fluid inclusions is less than 1 µm, thus limiting their observation and measurement. The fluid inclusions are two-phase liquid H<sub>2</sub>O–vapor H<sub>2</sub>O, with an average liquid–vapor ratio of 8:2 dominated by the liquid phase. Liquid-rich inclusions occasionally coexist with vapor-rich inclusions (Fig. 7a). In addition, fluid inclusions were not

**Table 2** Chemical composition of Ag-Se-S minerals determined by scanning electron microscope with energy-dispersive spectrometry (SEM-EDS)

No	Sample	<i>n</i>	Ag (wt%)	Se (wt%)	S (wt%)	Total (wt%)	Ag (at%)	Se (at%)	S (at%)	Total (at%)	Empirical formulae
1	T-P02-15	7	79.1	17.5	3.4	100.0	69.1	20.9	10.0	100.0	Ag <sub>2.1</sub> (Se <sub>0.6</sub> S <sub>0.3</sub> ) <sub>0.9</sub>
2	T-P02-17	172	79.5	15.9	4.7	100.0	68.0	18.5	13.5	100.0	Ag <sub>2.0</sub> (Se <sub>0.6</sub> S <sub>0.4</sub> ) <sub>1.0</sub>
3	T-P40-09	66	77.9	19.0	3.1	100.0	68.2	22.7	9.1	100.0	Ag <sub>2.1</sub> (Se <sub>0.7</sub> S <sub>0.3</sub> ) <sub>1.0</sub>
4	T-P40-27	5	78.9	17.6	3.5	100.0	68.9	21.0	10.1	100.0	Ag <sub>2.1</sub> (Se <sub>0.6</sub> S <sub>0.3</sub> ) <sub>0.9</sub>
5	T-P40-29	55	78.3	18.7	3.0	100.0	68.7	22.5	8.8	100.0	Ag <sub>2.1</sub> (Se <sub>0.7</sub> S <sub>0.3</sub> ) <sub>1.0</sub>
6	T-P40-34	90	77.8	18.9	3.3	100.0	67.9	22.5	9.6	100.0	Ag <sub>2.0</sub> (Se <sub>0.7</sub> S <sub>0.3</sub> ) <sub>1.0</sub>

**Table 3** Chemical composition of Ag-sulfosalts determined by scanning electron microscope with energy-dispersive spectrometry (SEM-EDS)

No	Sample	<i>n</i>	Ag (wt%)	Cu (wt%)	Zn (wt%)	Fe (wt%)	Sb (wt%)	Ge (wt%)	Se (wt%)	S (wt%)	Total (wt%)
Pyrargyrite											
1	02-15	3	60.3	—	—	—	22.4	—	3.1	15.2	100.0
2	40-09	1	60.1	—	—	—	22.1	—	1.4	16.4	100.0
Selenopolybasite											
1	02-15	13	68.4	2.7	—	—	9.8	—	9.1	10.0	100.0
2	02-17	17	69.1	3.1	—	—	9.7	—	6.7	11.4	100.0
3	40-09	6	69.5	2.1	—	—	9.6	—	7.3	11.5	100.0
4	40-34	28	68.9	3.6	—	—	9.4	—	6.6	11.5	100.0
Freibergite											
1	02-15	20	32.3	15.5	2.1	4.4	25.9	—	6.4	19.4	100.0
2	40-34	8	20.7	22.5	2.7	3.8	27.6	—	—	22.7	100.0
Argyrodite											
1	02-15	1	73.7	—	—	—	—	5.1	10.2	11.0	100.0
2	02-17	5	73.9	—	—	—	—	5.5	8.0	12.6	100.0

No	Sample	<i>n</i>	Ag (at%)	Cu (at%)	Zn (at%)	Fe (at%)	Sb (at%)	Ge (at%)	Se (at%)	S (at%)	Total (at%)	Empirical formulae
Pyrargyrite												
1	02-15	3	44.9	—	—	—	14.8	—	2.1	38.2	100.0	Ag <sub>3.1</sub> Sb <sub>1.0</sub> (Se <sub>0.2</sub> S <sub>2.7</sub> ) <sub>2.9</sub>
2	40-09	1	44.0	—	—	—	14.3	—	1.4	40.3	100.0	Ag <sub>3.1</sub> Sb <sub>1.0</sub> (Se <sub>0.1</sub> S <sub>2.8</sub> ) <sub>2.9</sub>
Selenopolybasite												
1	02-15	13	53.4	3.1	—	—	6.8	—	9.9	26.8	100.0	(Ag <sub>15.5</sub> Cu <sub>0.9</sub> ) <sub>16.4</sub> Sb <sub>2.0</sub> (Se <sub>2.9</sub> S <sub>7.8</sub> ) <sub>10.7</sub>
2	02-17	17	53.0	4.0	—	—	6.6	—	7.0	29.4	100.0	(Ag <sub>15.4</sub> Cu <sub>1.2</sub> ) <sub>16.6</sub> Sb <sub>1.9</sub> (Se <sub>2.0</sub> S <sub>8.5</sub> ) <sub>10.5</sub>
3	40-09	6	53.3	2.8	—	—	6.5	—	7.4	29.7	100.0	(Ag <sub>15.5</sub> Cu <sub>0.8</sub> ) <sub>16.3</sub> Sb <sub>1.9</sub> (Se <sub>2.2</sub> S <sub>8.6</sub> ) <sub>10.8</sub>
4	40-34	28	52.0	4.6	—	—	6.4	—	7.0	29.7	100.0	(Ag <sub>15.2</sub> Cu <sub>1.3</sub> ) <sub>16.5</sub> Sb <sub>1.9</sub> (Se <sub>2.0</sub> S <sub>8.6</sub> ) <sub>10.6</sub>
Freibergite												
1	02-15	20	20.5	16.5	2.0	5.4	14.4	—	0.9	40.3	100.0	(Ag <sub>5.7</sub> Cu <sub>4.8</sub> ) <sub>10.5</sub> (Zn <sub>0.6</sub> Fe <sub>1.6</sub> ) <sub>2.2</sub> Sb <sub>4.0</sub> (Se <sub>0.2</sub> S <sub>11.3</sub> ) <sub>11.5</sub>
2	40-34	8	12.1	22.2	2.6	4.3	14.3	—	—	44.6	100.0	(Ag <sub>3.4</sub> Cu <sub>6.4</sub> ) <sub>9.8</sub> (Zn <sub>0.8</sub> Fe <sub>1.2</sub> ) <sub>2.0</sub> Sb <sub>4.0</sub> S <sub>12.5</sub>
Argyrodite												
1	02-15	1	55.7	—	—	—	—	5.7	10.5	28.1	100.0	Ag <sub>1.7</sub> Ge <sub>0.2</sub> (Se <sub>0.3</sub> S <sub>0.8</sub> ) <sub>1.1</sub>
2	02-17	5	54.6	—	—	—	—	6.0	8.1	31.4	100.0	Ag <sub>1.6</sub> Ge <sub>0.2</sub> (Se <sub>0.2</sub> S <sub>0.9</sub> ) <sub>1.1</sub>

found in quartz, which is generally microcrystalline and cryptocrystalline in size.

The final melting temperature of the fluid inclusions ( $T_m$ ) ranges from  $-0.1^\circ$  to  $-1.5^\circ\text{C}$ , and the mode lies on an interval from  $0.0^\circ$  to  $-0.4^\circ\text{C}$ . These values are equal to 0.1–2.6 wt% NaCl eq. and 0.3–0.7 wt% NaCl eq., respectively. The homogenization temperature ( $T_h$ ) of these fluid inclusions ranges from 150 to  $270^\circ\text{C}$  with the mode within an interval from 240 to  $250^\circ\text{C}$  (Fig. 7b).

## 5. Discussion

### 5.1 Vein textures

Dong *et al.* (1995) and Morrison *et al.* (1990) discussed three major classes of vein textures reflecting their

possible origin, that is, primary growth, recrystallization, and replacement textures. With respect to this classification, vein textures occurring in the RRZ are assigned to these classes. Primary growth textures include massive, micro-comb, moss, colloform, and crustiform types. Recrystallization textures are represented by mosaic, feathery, and flamboyant types. Replacement textures include lattice bladed and ghost bladed types.

The massive texture was initiated by the precipitation of chalcedony from a hydrothermal fluid, which was in an intermediate silica supersaturation with respect to quartz at low temperatures ( $<180^\circ\text{C}$ ). Low crystallinity maintained during and after the deposition suggests that chalcedony has not been exposed to temperatures higher than  $180^\circ\text{C}$  (Morrison *et al.*,

**Table 4** Chemical composition of Ag-bearing chalcopyrite and sphalerite determined by scanning electron microscope with energy-dispersive spectrometry (SEM-EDS)

No	Sample	n	Cu (wt%)	Zn (wt%)	Fe (wt%)	Ag (wt%)	S (wt%)	Total (wt%)	Cu (at%)	Zn (at%)	Fe (at%)	Ag (at%)	S (at%)	Total (at%)	Empirical formulae
<b>Chalcopyrite</b>															
1	40-29	4	30.5	—	27.3	9.1	33.1	100.0	23.0	—	23.4	4.1	49.5	100.0	Cu <sub>0.9</sub> Fe <sub>0.9</sub> Ag <sub>0.2</sub> S <sub>2.0</sub>
<b>Sphalerite</b>															
1	02-15	3	—	62.6	2.1	—	35.3	100.0	—	45.7	1.8	—	52.5	100.0	(Zn <sub>0.9</sub> Fe <sub>0.0</sub> ) <sub>0.9</sub> S <sub>1.1</sub>
2	40-09	14	—	63.2	2.7	—	34.1	100.0	—	46.5	2.3	—	51.2	100.0	(Zn <sub>0.9</sub> Fe <sub>0.1</sub> ) <sub>1.0</sub> S <sub>1.0</sub>
3	40-34	11	—	63.9	2.1	—	34.0	100.0	—	47.2	1.8	—	51.0	100.0	(Zn <sub>0.9</sub> Fe <sub>0.0</sub> ) <sub>0.9</sub> S <sub>1.0</sub>

1990). Once the massive chalcedony vein was exposed to the higher temperatures (<180°C), it recrystallized to form massive microcrystalline quartz that shows mosaic textures (Lovering, 1972; Dong *et al.*, 1995). In addition, crystalline quartz in vugs of massive chalcedony resulted from void fillings by a later fluid (Bodnar *et al.*, 1985).

The micro-comb texture is considered a product of geometrical selection. In this process, only crystals in the direction of maximum growth rate perpendicular to the existing surface were formed. Slow changing conditions were necessary to form micro-comb quartz in open space (Dong *et al.*, 1995). The micro-comb precipitation required slight supersaturation with respect to quartz (Fournier, 1985). The presence of a micro-comb texture in the vein edge and massive chalcedony in the vein center reflects a shift of fluid conditions from slightly quartz-supersaturated to intermediate quartz-supersaturated.

The moss and colloform textures are indicative of the initial precipitation of amorphous silica (Dong *et al.*, 1995) from a high-degree silica-supersaturated fluid (Weres *et al.*, 1982). The precipitation of amorphous silica in these textures was controlled by surface tension, which tended to attain a spherical shape for minimum free energy configuration (Rogers, 1917; Adams, 1920). Another process that may have controlled the formation of these textures was the segregation of impurities at a very slow diffusion rate than that of crystal growth (Adams, 1920; Oehler, 1976). The independent and interconnected spheres in the moss and colloform textures, respectively, resulted from the difference in nuclei sites (Dong *et al.*, 1995). The moss texture formed from suspended nuclei sites in silica gel, while the colloform texture formed from nuclei sites that attached to the wall rocks and earlier veins. In the shallow portion, amorphous silica in the colloform textures was recrystallized to fibrous chalcedony with a rounded surface. Following this step, quartz with radial extinction formed, resulting in the flamboyant texture (Adams, 1920; Dong *et al.*, 1995). In addition to the flamboyant texture, the feathery texture was identified as a recrystallization product of the colloform bands. The feathery appearance of the recrystallized colloform reflects the growth of fibrous chalcedony on initial colloform spheres that acted as a growth surface (Rimstidt & Cole, 1983). The feathery texture implies an intermediate stage or imperfect recrystallization and was restricted to the surficial environment (Adams, 1920; Morrison *et al.*, 1990).

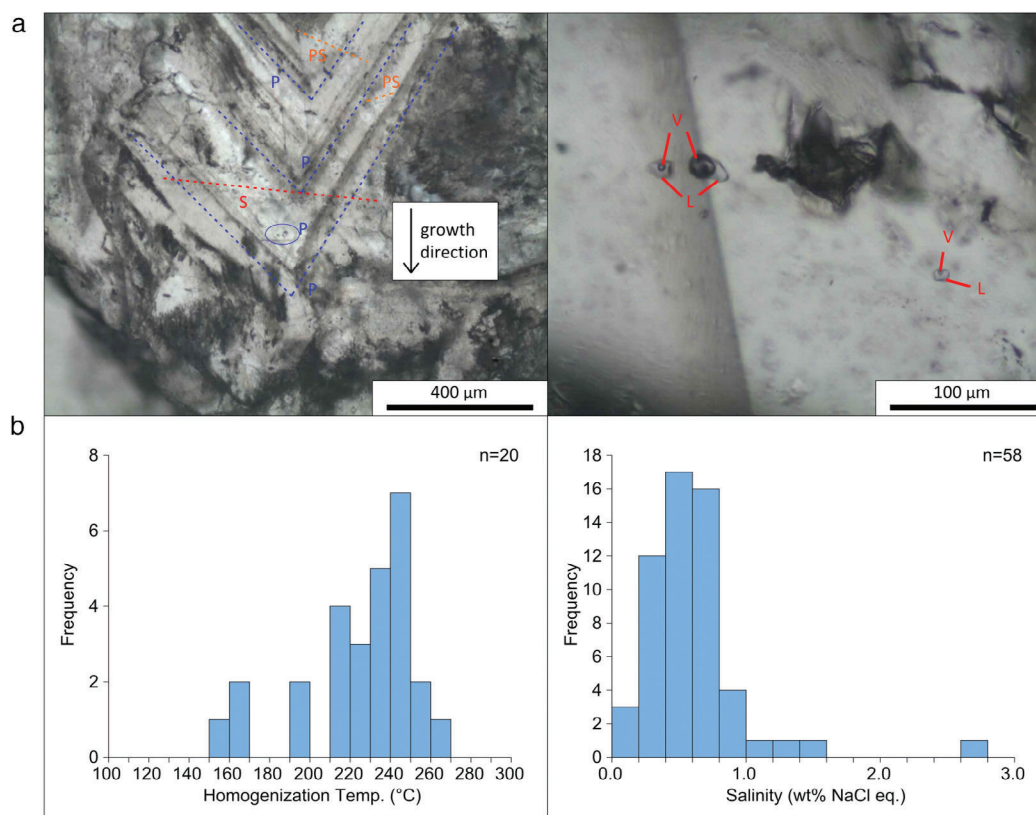


**Fig. 7** (a) Photomicrographs of primary fluid inclusions in the growth zone of calcite cut by pseudosecondary and secondary fluid inclusions. Liquid- and vapor-rich inclusions coexist. (b) Data distribution of homogenization temperature and salinity of fluid inclusions of late-stage calcite at the River Reef Zone (T-P02-15, DD96PA02, depth 108.10 m). Abbreviations: P, primary; PS, pseudosecondary; S, secondary; L, liquid; V, vapor.

Buchanan (1981) stated that the crustiform texture was a characteristic of veins formed in the epithermal environment. Episodic pressure release due to reopening of fractures allowed boiling to take place. The presence of the ghost bladed and lattice bladed bands in the crustiform texture suggests that boiling occurred in the RRZ (Morrison *et al.*, 1990). The successive micro-comb and massive textures that follow the ghost bladed and lattice bladed textures indicate a reopening of the vein as the main factor of repetitive bands in the crustiform texture (Dong *et al.*, 1995). The massive chalcedony, moss, and colloform textures existing at the center of the veins and the low crystallinity degree suggest that the temperature of hydrothermal fluid decreased during the formation of the veins (Fournier, 1985). In addition, the variation of dominant minerals between calcite and quartz in this texture suggests that the crustiform texture in the RRZ also resulted from the fluctuation of hydrothermal fluid conditions.

The lattice bladed, ghost bladed, and parallel bladed textures are considered textural manifestation of boiling. Platy calcite displaying these textures is a diagnostic feature of boiling environment (Simmons & Christenson, 1994). In the lattice bladed texture, a large amount of calcite was precipitated from calcite-supersaturated fluids under gas-rich, open system, isothermal boiling conditions (Dong *et al.*, 1995) due to a decrease of partial pressure of  $\text{CO}_2$  (Ellis, 1959). As the solubility of calcite and quartz is retrogressive and progressive with respect to temperature change, respectively (Seward *et al.*, 2014), subsequent slow fluid cooling changed fluid conditions to calcite-undersaturated and slightly silica-supersaturated conditions. As the fluid became more supersaturated with respect to silica, microcrystalline quartz and chalcedony were precipitated, and calcite was partially redissolved and replaced. If the initial calcite was coarse grains and irregular, replacement took place along cleavages of calcite in a large

number of nuclei, which resulted in the reticular structure of the saccharoidal texture (Adams, 1920). In the ghost bladed and parallel bladed textures, fluid conditions were supersaturated with respect to calcite and quartz due to boiling with rapid cooling (Dong *et al.*, 1995). In this case, platy calcite and quartz were precipitated simultaneously.

The precipitation of amorphous silica and chalcedony, which were partially recrystallized to microcrystalline and crystalline quartz, suggests that the temperature of hydrothermal fluid was lower than 180°C (Morrison *et al.*, 1990). However, the temperature mode recorded by the fluid inclusions indicates that the gold mineralization took place at 240–250°C, which exceeded the temperature range favorable for the precipitation of amorphous silica and chalcedony. This discrepancy suggests the fluctuation of hydrothermal fluid in terms of its temperatures as documented by the presence of crustiform texture in the RRZ.

## 5.2 Physicochemical condition of ore-forming fluid

### 5.2.1 Sulfur fugacity

The examination of sulfur fugacity ( $fS_2$ ) is critical as most of the ore minerals occur as sulfides. A diagram of  $\log fS_2$ -temperature suggested by Barton Jr. and Toulmin III (1964) was used to deduce  $fS_2$  of the ore-forming fluid. Several lines representing equilibrium reaction were incorporated within the diagram to confirm the estimated results. The contours of the Ag fraction ( $X_{Ag}$ ) of electrum were constructed between the sulfur condensation and  $Ag_2S$ -Ag- $S_2$  equilibrium lines. According to the ore mineral assemblages, the early stage was marked by the presence of naumannite-aguilarite, chalcopryrite, pyrite, marcasite, sphalerite, and pyrrhotite coexisting with electrum of 69 Ag at%. Plotting on the diagram estimated a formation temperature of approximately 290°C with a  $\log fS_2$  of nearly -11.3 (Fig. 8a).

The  $fS_2$  in the late stage was evaluated by plotting the Ag content of electrum precipitated in this stage and the homogenization temperature of fluid inclusions. The Ag content of electrum at this stage ranges from 58 to 61 at%, and the homogenization temperature of fluid inclusions is 250°C.  $\log fS_2$  of the late stage is correspondingly -11.8 (Fig. 8a). The result of the late stage is consistent with the presence of chalcopryrite and pyrite and the lack of pyrrhotite. The

apparent  $fS_2$  value decreased from the early to late stages. However, the  $fS_2$  effect increased relative to the  $Ag_2S$  buffer due largely to the temperature decrease. The positive gradient of  $X_{Ag}$  contours and the fluctuation of the ore-forming fluid conditions as suggested by the discrepancy between homogenization temperature and precipitation temperature of amorphous silica and chalcedony may have amplified the difference of apparent  $fS_2$  value between the early and the late stages.

### 5.2.2 Selenium fugacity

Selenium fugacity ( $fSe_2$ ) is an integral part of research studies to understand geochemical significance of ore mineral assemblages containing selenium (Simon & Essene, 1996). In the RRZ, Se was encountered in several ore minerals: naumannite-aguilarite, selenopolybasite, argyrodite, freibergite, and pyrrargyrite. The evaluation of  $fSe_2$  was carried out using a  $\log fSe_2$ -temperature diagram proposed by Simon and Essene (1996). The construction of the diagram took into account the contours of the Ag fraction ( $X_{Ag}$ ) of electrum between the formation of naumannite from Ag and  $Se_2$  gas and the Se condensation line.

The points were plotted based on the Ag content of electrum and the formation temperatures of both stages. The  $X_{Ag}$  of electrum in the early stage is 0.7, and the estimated formation temperature is 290°C, while the  $X_{Ag}$  of electrum in the late stage is 0.6, and the homogenization temperature is 250°C.  $\log fSe_2$  of the early and late stages is approximately -13.5 and -14.1, respectively (Fig. 8b). Similar to  $fS_2$ , the  $fSe_2$  effect also increased during the progressive ore deposition due to the temperature decrease, although the apparent  $fS_2$  value decreased. The difference of the apparent  $fSe_2$  value between the early and the late stages may have been enlarged due to the positive slope of  $X_{Ag}$  contours and the discrepancy between the homogenization temperature and precipitation temperature of amorphous silica and chalcedony.

### 5.2.3 Phase relations

Phase relations were examined on the  $\log fSe_2$ - $fS_2$  diagrams constructed at 250 and 300°C (Fig. 8c,d). The latter diagram was used to approximate the phase relations in the early stage as thermochemical data at 290°C are unavailable. The  $\log fSe_2$ - $fS_2$  diagrams were simplified by omitting several equilibrium reactions that are not encountered in the RRZ. The reactions involving pyrite, pyrrhotite, chalcopryrite, and bornite

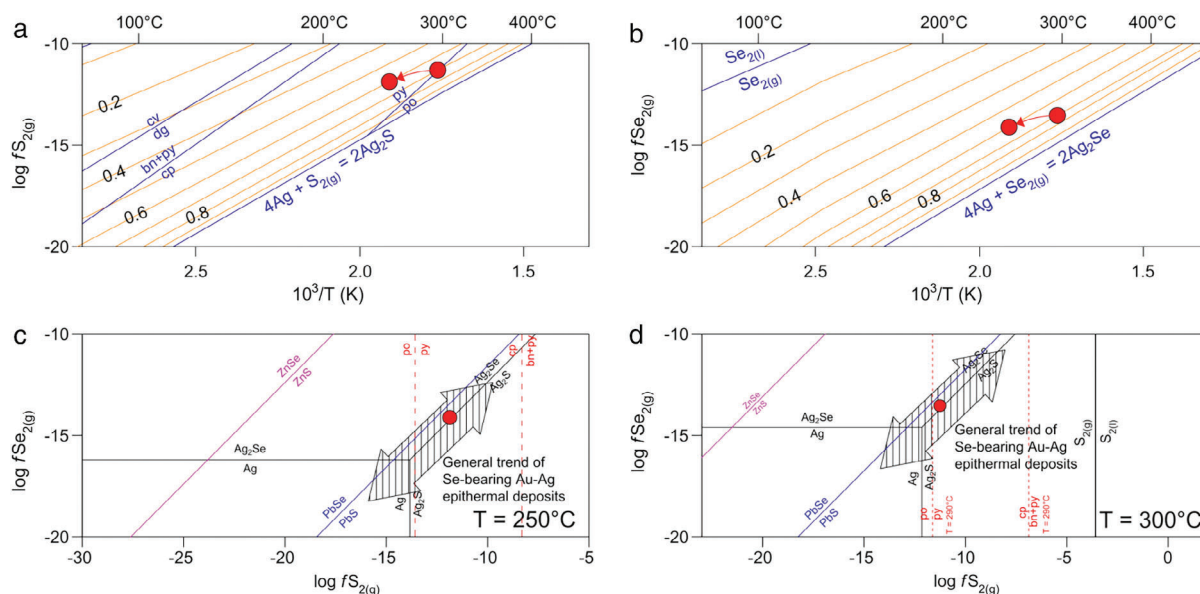


**Fig. 8** (a) Log  $fS_2$  and (b) log  $fSe_2$  against temperature in the early and late stages. Phase relations of native-sulfide-selenide minerals at temperatures of (c) 250°C and (d) 300°C and their relationships to the general trends of Se-bearing Au–Ag epithermal deposits (modified after Simon *et al.*, 1997).

are considered the sulfide buffer reactions and are presented in the diagrams. As the thermochemical data of those buffer reactions at 290°C are available, the buffer equilibrium lines were depicted on the second diagram instead of the lines representing the reactions at 300°C.

Each pair of sulfur and selenium fugacity lies on the equilibrium line between naumannite and argentite. These results are characterized by  $fSe_2/fS_2$  lower than unity. In this case, Se is more favorable for the crystallographic replacement of S as indicated by the results of the semiquantitative analysis of the ore minerals. Although the ore-forming fluid was relatively Se-rich, the early substitution of S by Se may have inhibited Se enrichment in the remaining ore-forming fluid. Consequently, selenide minerals other than Ag–Se–S minerals were not precipitated. In addition, the plotting of  $fSe_2$  and  $fS_2$  in the RRZ, which lies on the equilibrium line between naumannite and argentite, is consistent with the general trend of Se-bearing Au–Ag epithermal deposits (Simon *et al.*, 1997).

### 5.3 RRZ and exploration in the Palu area

The vein textures and ore mineralogy in the RRZ deposit agree with characteristics of low-sulfidation epithermal deposits (Dong *et al.*, 1995; Simmons *et al.*,

2005). Likewise, the results of fluid inclusion microthermometry in the RRZ ( $T_h = 240\text{--}250^\circ$ , salinity = 0.3–0.7 wt% NaCl eq.) overlap with the typical ranges of temperature and salinity of ore-forming fluids in the epithermal environment (Wilkinson, 2001). The presence of several occurrences of gold placer deposit along the transcurrent PKFZ serving as a hydrothermal fluid pathway (van Leeuwen & Pieters, 2011) and the presence of the RRZ deposit imply that the regions around the PKFZ are potential areas of exploration of epithermal deposits.

## 6. Conclusions

Quartz-carbonate veins in the RRZ display primary growth, recrystallization, and replacement textures, such as massive, micro-comb, moss, colloform, crustiform, mosaic, feathery, flamboyant, lattice bladed, ghost bladed, parallel bladed, and saccharoidal textures. These textures reflect the initial precipitation of amorphous silica, its transformation to more stable phase, and boiling. Mineralized quartz-carbonate veins contain electrum, naumannite-aguilarite, chalcopyrite, sphalerite, galena, pyrite, marcasite, and pyrrhotite precipitated in the early stage. Apart from pyrrhotite, the mineralized veins host these minerals along with selenopolybasite, freibergite, argyrodite,

pyrrargyrite, and galena precipitated in the late stage. The ore minerals were precipitated at 290 and 250°C in the early and late stages, respectively. In both stages, Se occurs as the crystallographic replacement of S.

## Acknowledgments

The authors thank the management and staff of PT Bumi Resources Minerals, Tbk. for permission and support during the field survey, discussion, and for supplementary information regarding this research. We are deeply grateful to Dr. Thomas Tindell and members of Laboratory of Economic Geology, Kyushu University, for their assistance in sample preparation and advice on data interpretation. We also thank the two anonymous reviewers of *Resource Geology* for their invaluable suggestions to improve the manuscript. This project was partially funded by the Advanced Graduate Program in Global Strategy for Green Asia (New Frontier Leading Program awarded to Kyushu University). The authors received financial support from Advanced Graduate Program in Global Strategy for Green Asia for the fieldwork.

## Author contributions

Tomy Alvin Rivai, Kotaro Yonezu, and Syafrizal developed the concepts, designed this study, and carried out the fieldwork under the guidance of Damar Kusumanto. Tomy Alvin Rivai conducted laboratory analyses under the guidance of Kotaro Yonezu and Kenzo Sanematsu. Tomy Alvin Rivai wrote the manuscript with contributions on interpretation and discussion of the results from Kotaro Yonezu, Syafrizal, Kenzo Sanematsu, Damar Kusumanto, Akira Imai, and Koichiro Watanabe. All authors read and commented on the manuscript.

## References

- Adams, S. F. (1920) A microscopic study of vein quartz. *Econ. Geol.*, 15, 623–664.
- Barton, P. B. Jr. and Toulmin, P. III (1964) The electrom-tarnish method for the determination of the fugacity of sulfur in laboratory sulfide systems. *Geochim. Cosmochim. Acta*, 28, 619–640.
- Bates, R. L. and Jackson, J. A. (1987). *Glossary of geology*. American Geological Institute, Alexandria, VA, 788p.
- Bodnar, R. J. (1993) Revised equation and table for determining the freezing point depression of H<sub>2</sub>O–NaCl solutions. *Geochim. Cosmochim. Acta*, 57, 683–684.
- Bodnar, R. J., Reynolds, T. J. and Kuehn, C. A. (1985) Fluid inclusion systematics in epithermal systems. In Berger, B. R. and Bethke, P. M. (eds.) *Geology and geochemistry of epithermal systems*. *Rev. Econ. Geol.*, Vol. 2, El Paso, TX, 73–97.
- Buchanan, L. J. (1981) Precious metal deposits associated with volcanic environments in the southwest. *Ariz. Geol. Soc. Digest*, 14, 237–262.
- Carlile, J. C., Digwodiogo, S. and Darius, K. (1990) Geological setting, characteristics, and regional exploration for gold in the volcanic arcs of North Sulawesi, Indonesia. *J. Geochem. Explor.*, 35, 105–140.
- Dong, G., Morrison, G. and Jaireth, S. (1995) Quartz textures in epithermal veins, Queensland—Classification, origin, and implication. *Econ. Geol.*, 90, 1841–1856.
- Ellis, A. J. (1959) The solubility of calcite in carbon dioxide solutions. *Amer. J. Sci.*, 257, 354–365.
- Fournier, R. O. (1985) The behavior of silica in hydrothermal solutions. In Berger, B. R. and Bethke, P. M. (eds.) *Geology and geochemistry of epithermal systems*. *Rev. Econ. Geol.*, 2, El Paso, TX, 45–61.
- Hall, H. T. (1967) The pearceite and polybasite series. *Am. Mineral.*, 52, 1311–1321.
- Helmerts, H., Maaskant, P. and Hartel, T. H. D. (1990) Garnet peridotite and associated high-grade rocks from Sulawesi, Indonesia. *Lithos*, 25, 171–188.
- Katili, J. A. (1970) Large transcurrent faults in Southeast Asia with special reference to Indonesia. *Geol. Rundschau*, 59, 581–600.
- Kavalieris, I., Walshe, J. L., Halley, S. and Harrold, B. P. (1990) Dome-related gold mineralization of the Tombulilato district, North Sulawesi, Indonesia. *Econ. Geol.*, 85, 1208–1225.
- Kavalieris, I., van Leeuwen, T. M. and Wilson, M. (1992) Geological setting and styles of mineralization, north arm of Sulawesi, Indonesia. *J. Southeast Asian Earth Sci.*, 7, 113–129.
- Lovering, T. G. (1972) Jasperoid in the United States – Its characteristics, origin, and economic significance. *U.S. Geological Survey professional paper 710*, Washington, DC, 164p.
- Morrison, G., Guoyi, D. and Jaireth, S. (1990). Textural zoning in epithermal quartz veins. *Klondike Exploration Services*, Townsville, Queensland, Australia, 1–21.
- Oehler, J. H. (1976) Hydrothermal crystallization of silica gel. *Geol. Soc. Amer. Bull.*, 87, 1143–1152.
- Perelló, J. (1994) Geology, porphyry Cu–Au, and epithermal Cu–Au–Ag mineralization of the Tombulilato district, North Sulawesi, Indonesia. *J. Geochem. Explor.*, 50, 221–256.
- Petruk, W., Owens, D. R., Stewart, J. M. and Murray, E. J. (1974). Observations on acanthite, aguilarite and naumannite. *Can. Min.*, 12, 365–369.
- Phillips, W. R. and Griffen, D. T. (1981). *Optical mineralogy: the nonopaque minerals*. W. H. Freeman and Company, San Francisco, CA, 677p.
- Rimstidt, J. D. and Cole, D. R. (1983) Geothermal mineralization I: The mechanism of formation of the Beowawe, Nevada, siliceous sinter deposit. *Amer. J. Sci.*, 283, 861–875.
- Rogers, A. F. (1917) A review of the amorphous minerals. *J. Geol.*, 25, 515–541.
- Seward, T. M., William-Jones, A. E. and Migdisov, A. A. (2014) The chemistry of metal transport and deposition by ore-

- forming hydrothermal fluids. In Scott, S. D. (ed.) Treatise on geochemistry, Vol. 13, Elsevier, Amsterdam, 29–57.
- Simmons, S. F. and Christenson, B. W. (1994) Origins of calcite in a boiling geothermal system. *Amer. J. Sci.*, 294, 361–400.
- Simmons, S. F., White, N. C. and John, D. A. (2005) Geological characteristics of epithermal precious and base metal deposits. In Hedenquist, J. W., Thompson, J. F. H., Goldfarb, R. J. and Richards, J. P. (eds.) Economic geology 100th anniversary volume, Economic Geology Publishing Company, El Paso, 485–522p.
- Simon, G. and Essene, E. J. (1996) Phase relations among selenides, sulfides, tellurides and oxides: I. thermodynamic properties and calculated equilibria. *Econ. Geol.*, 91, 1183–1208.
- Simon, G., Kesler, S. E. and Essene, E. J. (1997) Phase relations among selenides, sulfides, tellurides and oxides: I. applications to selenide-bearing ore deposits. *Econ. Geol.*, 92, 468–484.
- Sukanto, R. A. B., Sumadirdja, H., Suptandar, T., Hardjoprawiro, S. and Sudana, D. (1973). Reconnaissance geological map of the Palu Quadrangle, Sulawesi, 1:250,000. Geological Research and Development Centre, Bandung, Indonesia.
- Syafrizal, Rivai, T. A., Yonezu, K., Kusumanto, D., Watanabe, K. and Hede, A. N. H. (2017) Characteristics of a low-sulfidation epithermal deposit in the river reef zone and the Watuputih Hill, the Poboya gold prospect, Central Sulawesi, Indonesia: Host rocks and hydrothermal alteration. *Minerals*, 7, 124.
- Thompson, A. J. B. and Thompson, J. F. H. (1996). Atlas of alteration: a field and petrographic guide to hydrothermal alteration minerals. Mineral Deposit Division, Geological Association of Canada, Newfoundland, Canada, 36.
- Turner, S. J., Flindell, P. A., Hendri, D., Hardjana, I., Lauricella, P. F., Lindsay, R. P., Marpaung, B. And White, G. P. (1994) Sediment-hosted gold mineralisation in the Ratatokok district, North Sulawesi, Indonesia. *J. Geochem. Explor.*, 50, 317–336.
- Van Leeuwen, T. M. (1994) 25 years of mineral exploration and discovery in Indonesia. *J. Geochem. Explor.*, 50, 13–90.
- Van Leeuwen, T. M. and Muhardjo (2005) Stratigraphy and tectonic setting of the cretaceous and Paleogene volcanic-sedimentary successions in Northwest Sulawesi, Indonesia: Implications for the Cenozoic evolution of Western and northern Sulawesi. *J. Asian Earth Sci.*, 25, 481–511.
- Van Leeuwen, T. M. and Pieters, P. E. (2011) Mineral deposits of Sulawesi. In Proceedings of the Sulawesi Mineral Resources 2011 Seminar MGEI-IAGI. Manado. Masyarakat Geologi Ekonomi, Indonesia, 1–109.
- Van Leeuwen, T.M., Allen, C. M., Kadarusman, A., Elburg, M., Palin, J. M., Muhardjo and Suwijanto (2007) Petrologic, isotopic, and radiometric age constraints on the origin and tectonic history of the Malino Metamorphic Complex, NW Sulawesi, Indonesia. *J. Asian Earth Sci.*, 29, 751–777.
- Van Leeuwen, T. M., Allen, C. M., Elburg, M., Massonne, H., Palin, J. M. and Hennig, J. (2016) The Palu metamorphic complex, NW Sulawesi, Indonesia: Origin and evolution of a young metamorphic terrane with links to Gondwana and Sundaland. *J. Asian Earth Sci.*, 115, 133–152.
- Wajdi, M. F., Santoso, B. S. T. J., Kusumanto, D. and Digwodiogo, S. (2012) Metamorphic hosted low sulphidation epithermal gold system at Poboya, Central Sulawesi: A general descriptive review. *Maj. Geol. Indones.*, 27, 131–141.
- Weres, O., Yee, A. and Tsao, L. (1982) Equations and type curves for predicting the polymerization of amorphous silica in geothermal brines. *Soc. Petrol. Eng. J.*, 22, 9–16.
- Wilkinson, J. J. (2001) Fluid inclusions in hydrothermal ore deposits. *Lithos*, 55, 229–272.
- Wisanggono, A., Abaijah, P., Akiro, K., Pertiwi, D. and Sauzy, R. A. (2011) Supergene enriched, intrusion related low sulphidation deposit, binebase-bawone, North Sulawesi, Indonesia. In Proceedings of the Sulawesi Mineral Resources 2011 Seminar MGEI-IAGI. Manado, Masyarakat Geologi Ekonomi, Indonesia, 131–144.